1996ApJ...470..636L

THE ASTROPHYSICAL JOURNAL, 470:636–646, 1996 October 10
© 1996. The American Astronomical Society. All rights reserved. Printed in U.S.A.

DOPPLER ACOUSTIC DIAGNOSTICS OF SUBSURFACE SOLAR MAGNETIC STRUCTURE

C. LINDSEY[1] AND D. C. BRAUN[1]
Solar Physics Research Corporation, P.O. Box 26732, Tucson, AZ 85726-6732
S. M. JEFFERIES[1] AND M. F. WOODARD[1]
Bartol Research Institute, University of Delaware, Newark, DE 19716
Y. FAN AND Y. GU
National Solar Observatory, 950 North Cherry Avenue, Tucson, AZ 85726-6732
AND
S. REDFIELD
Tufts University, New England Conservatory of Music, Somerville, MA 02144
Received 1996 January 29; accepted 1996 May 2

ABSTRACT

We used the Bartol-NSO-NASA South Pole helioseismic observations of 1991 January to probe the subsurface structure of active regions to depths of ~15,000 km. The helioseismic signature we particularly examine is intended to register acoustic Doppler effects caused by horizontal flows associated with the active region. We propose to show that the Doppler acoustic signature of horizontal flows is particularly well suited for deep subsurface diagnostics in terms of vertical discrimination of the structure. This study is based primarily on observations of NOAA Active Regions 6431, 6432, 6440, and 6442 between 1991 January 1 and January 8. We interpret the acoustic signatures we find in terms of a general outflow of the solar medium surrounding the active region. The acoustic signatures are strongly dependent on wavenumber, which suggests an outflow that is quite weak near the surface, the upper 4000 km of the subphotosphere, but which increases strongly with depth to velocities of several hundred meters per second at 15,000 km. This depth profile evolves rapidly as the active region matures. Young active regions show a strong outflow signature for waves that explore depths between 4000 and 8000 km. As the active region matures, the outflow vacates these intermediate layers and submerges to depths mostly below 8000 km.

We examine the location of AR 6442 for a possible preemergence signature. We also show evidence for extended, relatively superficial flows in the quiet Sun between the active region bands directed roughly into the active region bands.

Subject headings: Sun: activity — Sun: interior — Sun: magnetic fields — Sun: oscillations

1. INTRODUCTION

The advent of helioseismology over the last 25 years has allowed us literally to look into the Sun, revolutionizing our understanding of the solar interior. Until relatively recently, helioseismic perspective has concentrated largely on global qualities of the solar interior structure, e.g., the overall temperature dependence with radius, and the rotation rate over fairly broad bands in latitude. However, a great deal of important solar physics occurs on local scales, particularly where magnetic structure and solar activity are concerned. The prospect of resolving subphotospheric magnetic structure could revolutionize our understanding of the solar dynamo and the solar activity cycle as well as our understanding of near-surface sunspot structure.

With improving observational instrumentation, local diagnostics have become a seriously exciting prospect. Braun, Duvall, & LaBonte (1988) and subsequently Bogdan et al. (1993) found that sunspots absorb acoustic waves, and this has given rise to a variety of interesting problems dealing with how waves behave in a sunspot atmosphere and how they interact with magnetic fields (Hollweg 1988; Lou 1990; Sakurai, Goossens, & Hollweg 1991; Spruit & Bogdan 1992; Calley & Bogdan 1993; Keppens, Bogdan, & Goossens 1994). It has also created considerable excitement about how such an effect can be exploited diagnostically (e.g., Lindsey & Braun 1990; Brown 1991; Braun et al. 1992). Braun (1995) has since determined the scattering phase shifts and mode-mixing amplitudes due to the acoustic refractive properties of sunspots. These and other developments (see review by Bogdan & Braun 1995) have made it clear that the time is ripe to develop the local perspective for helioseismology in a serious way. We are particularly intent on applying the tools of local helioseismology to the solar interior. We think that this offers the best possible prospect for an eventual understanding of the solar dynamo and the solar activity cycle.

2. BASIC PRINCIPLES

If the waves that we see on the solar surface interact with subsurface structure in any number of possible ways, it should be straightforward to use their surface signatures to "see" acoustically into the solar interior, just as our eyes use the oscillating electric field at the surfaces of our corneas to see into the electromagnetic environment, and inform us about objects and structures that interact with the electromagnetic field. In the case of helioseismic techniques, the methods are computational rather than optical and in their full rigor are computationally demanding. A broad variety of holographic and tomographic techniques have been pro-

[1] Visiting Astronomer, National Solar Observatory, NOAO. NOAO is operated by AURA, Inc. under cooperative agreement with the National Science Foundation.

© American Astronomical Society • Provided by the NASA Astrophysics Data System

1996ApJ...470..636L

posed (see, e.g., Lindsey & Braun 1990; Brown 1991; Braun et al. 1992). The analog to the function of our eyes with respect to light is what we call acoustic holography. This particular concept is introduced by Lindsey & Braun (1990) and discussed by Braun et al. (1992). The important point is that if solar interior structure manifests a significant acoustic signature of any kind on the surface, the tools for its analysis are available in the computational analogs of the functions of our eyes with respect to electromagnetic waves. The primary purpose of this study is to secure the acoustic signature itself.

The basic tool of local helioseismology in analogy with the function of our eyes is the acoustic power map (see Braun et al. 1992; Toner & LaBonte 1993). Examples are shown in Figure 1 (Plate 11), obtained from the Bartol-NSO-NASA South Pole observations of 1991 January. We have computed the acoustic power in K-line brightness oscillations as a function of location in 1 mHz bands centered at 3 mHz (Fig. 1*a*), 4 mHz (Fig. 1*b*), and 6 mHz (Fig. 1*c*) integrated over a 50 hr period. The time interval and location for these acoustic power maps are listed with other information in Table 1, run 3. Figure 1*d* shows a K-line image integrated over the same period. Most of the features shown in these maps, certainly the sharper ones, are certain to have a superficial origin. The strong deficits in acoustic power seen in active regions, particularly at 4 mHz, are thought to be due simply to a suppression of the response of the low chromosphere to oscillations in the plage atmosphere. A more diffuse component of the acoustic deficit seen at 3 mHz is thought to be due to absorption of waves by nearby active regions, particularly sunspots, as discovered by Braun et al. (1988). If subsurface magnetic structure similarly absorbed waves, we could expect a surface signature that, properly analyzed, would show the underlying structure of the absorbing magnetic region.

It now appears that absorption of waves by magnetic fields is substantially a surface phenomenon, not significantly characterized by subsurface magnetic structure. Maps of the surface acoustic flux in the neighborhood of emerging sunspots show no significant signature before the active region appears at the surface (Lindsey, Braun, & Jefferies 1996). This complicates detection of interior structure. Besides absorbing and emitting, strong magnetic regions may refract or scatter waves. Braun (1995) has shown that sunspots visible on the surface do strongly scatter acoustic waves, as characterized by a scattering matrix, particularly by the phase shift of the diagonal elements of the matrix. However, a purely scattering structure illuminated by diffuse radiation (acoustic or otherwise) appears essentially invisible in undiscriminated acoustic power, as white against a background of white to our eyes, for example. What is needed to detect scattering is a phase-sensitive diagnostic, optical analogs of which are found in phase-contrast microscopy (Zernike 1935) and Schlieren imaging (see Born & Wolf 1975, p. 425), for example.

TABLE 1

TIME SERIES

Run	Start (1991 UT)	End (1991 UT)	Cumulative Time (hr)
1.....	Jan 1 19:25	Jan 2 12:29	16.03
2.....	Jan 4 07:47	Jan 5 05:42	21.13
3.....	Jan 6 06:58	Jan 8 09:41	48.72
4.....	Jan 4 15:15	Jan 4 23:48	8.53

NOTE.—Carrington longitude of frame center: 158.88; solar latitude of frame center: −3.69.

3. PHASE DIAGNOSTICS

The solar atmosphere turns out to be conveniently amenable to phase diagnostics. A significant portion of the solar acoustic spectrum, particularly that which is approximately 5 minutes in period, is substantially confined between the surface and a deeper reflecting level, the depth of which depends on the surface wavelength for a particular frequency. Interference between reflected components of the wave, for any particular frequency, results in a concentration of the spatial acoustic spectrum into an array of thin rings, as for electromagnetic radiation in an etalon (see Born & Wolff 1975, p. 329).

Figure 2*a* (Plate 12) shows an image of the spectral acoustic power of the solar oscillations in run 3 of Table 1. We computed the Fourier transform of the oscillations over both time and space. The result is a complex data cube over three dimensions: the temporal frequency, ω, and the x- and y-components of $\boldsymbol{k}$, the spatial wavenumber. The image in Figure 2*a* shows the square of the amplitude of the Fourier transform in a narrow frequency band (width 0.03255 mHz) centered at 3.255 mHz. It clearly shows the etalon rings of the solar oscillations spectrum.

Perturbations in the medium between the reflecting layers distort the etalon rings. A large-scale refractive perturbation in the solar medium, for example, covering the entire region observed, simply contracts or expands the etalon rings. This perturbation is isolated by filtering the Fourier transform through a spectral mask of the form shown in Figure 2*b*. This particular mask is comprised of a series of annuli, each of whose outer boundaries is fashioned to split its respective etalon ring along its culmination. A contraction or expansion of the etalon ring results in an increase or decrease, respectively, of the acoustic power admitted by the mask. In practice, we also filter the same data cube through the compliment of the mask shown.

The point of the exercise described here is to represent the effect of the perturbations in the etalon rings in local, not spectral, perspective. This is accomplished simply by inverse Fourier transforming the filtered data cubes back to the spatial domain. The squares of the amplitudes of each data cube are then summed over the desired frequency band to obtain acoustic power maps.

Figure 3 (Plate 13) shows this technique applied to the 50 hr interval of South Pole observations used to make the acoustic power maps in Figure 1. Figure 3*a* shows the acoustic power map made from the lower k range of each ring; Figure 3*b* shows that from the upper. These acoustic power maps are now compared for a representation of the effect of the phase perturbations in terms of acoustic power locally refracted across the spectral boundaries defined by the masks. Figure 3*c* shows the total power (higher k plus lower k), and Figure 3*d* shows the difference (higher k minus lower k). Figures 3*c* and 3*d* have been smeared to a width of 0.03 solar radii for improved representation of detail on the scale of the active regions. The procedure we are illustrating can be thought of as a sort of numerical knife edge—in this case rather a spectral cookie cutter—for the discrimination of simple refractive perturbations in local perspective. It is, in fact, particularly designed to accomplish the optimum in spatial discrimination at the expense of the spectral.

© American Astronomical Society • Provided by the NASA Astrophysics Data System

1996ApJ...470..636L

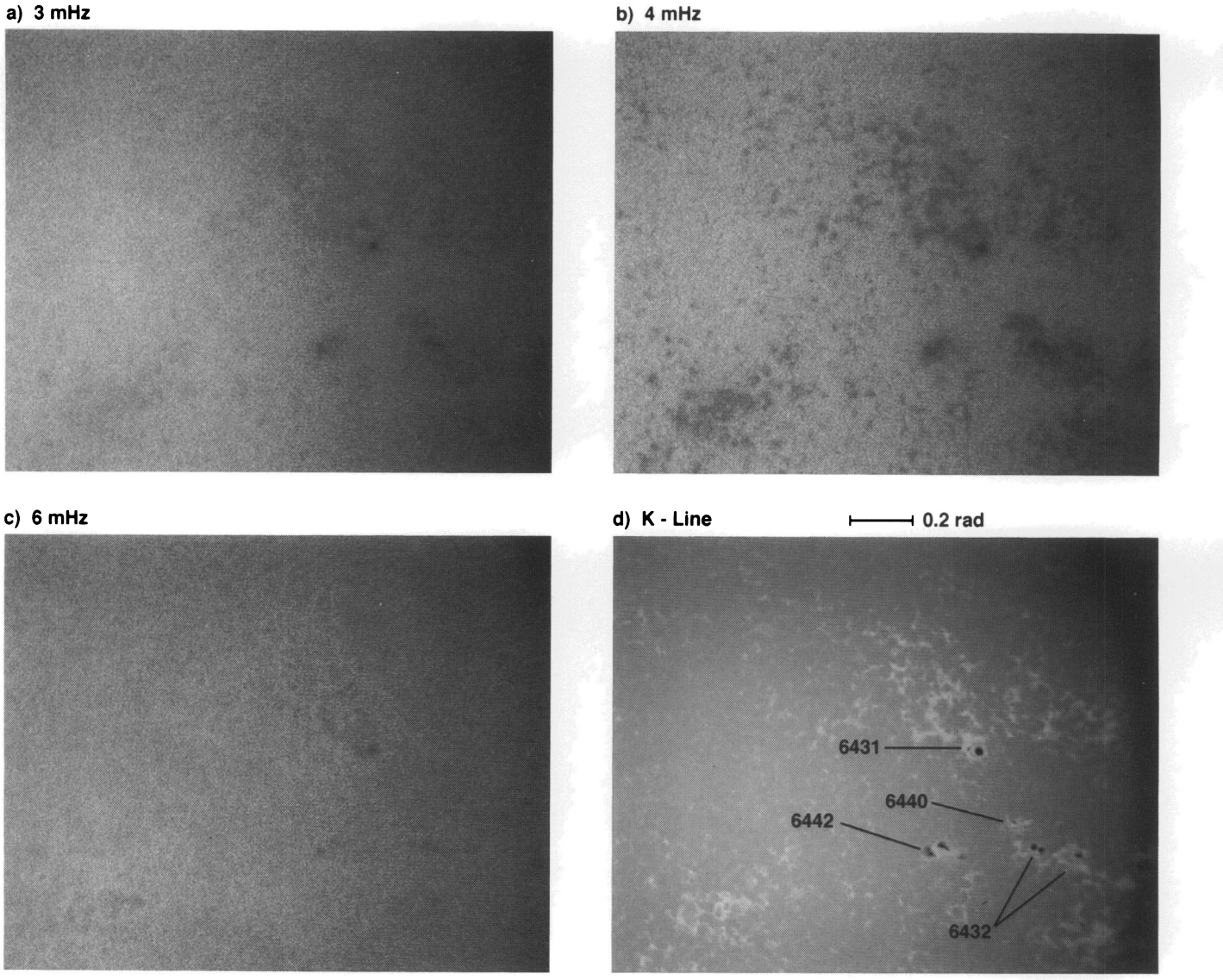

FIG. 1.—Acoustic power maps for 1 mHz bands centered at (*a*) 3, (*b*) 4, and (*c*) 6 mHz integrated over the 50 hr interval comprising run 3 in Table 1, determined from K-line images observed at 1 minute cadence from the South Pole. Frame (*d*) shows the K-line intensity averaged over the same 50 hr interval.

LINDSEY et al. (see 470, 637)

© American Astronomical Society • Provided by the NASA Astrophysics Data System

1996ApJ...470..636L

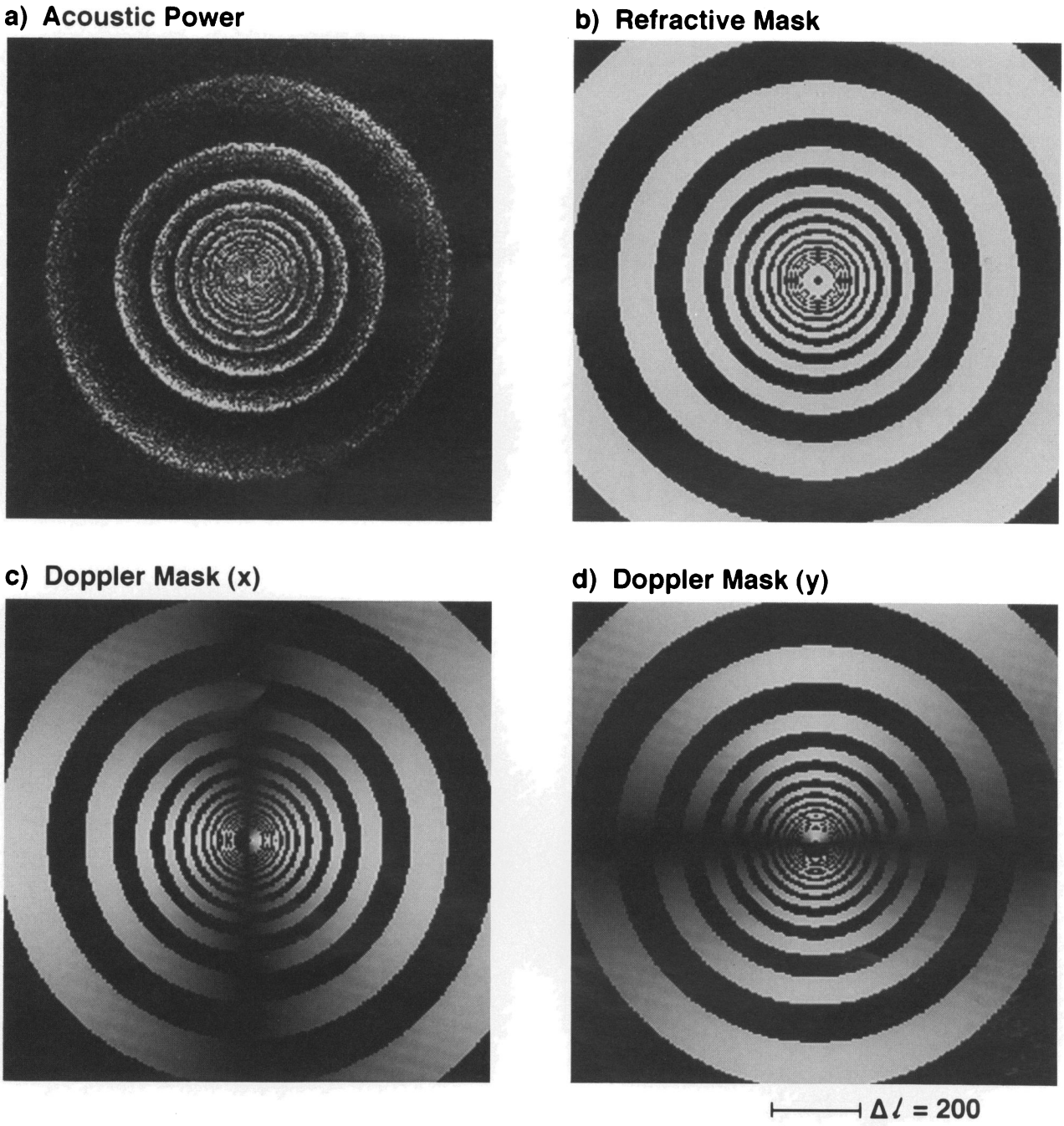

FIG. 2.—Spatial power spectrum of K-line brightness variations are shown for frequency 3.255 mHz over a bandwidth of 0.03255 mHz (*a*). Frame (*b*) shows the mask for knife-edge imaging of acoustic scattering by refractive structure. The mask shown admits the lower k annular domain of each etalon ring (white annuli). Its complement (not shown) admits the high-k annuli. Frame (*c*) shows the mask used for Doppler acoustic imaging of motion in the x-direction (longitude). Frame (*d*) shows the mask for motion in the y-direction (latitude). The complements of the masks in frames (*c*) and (*d*) are mirror reflections about the y- and x-axes, respectively. The scale for wavenumber, k, in this figure is indicated at lower right by a range of 200 in l, which is simply $2\pi k$.

LINDSEY et al. (see 470, 637)

© American Astronomical Society • Provided by the NASA Astrophysics Data System

1996ApJ...470..636L

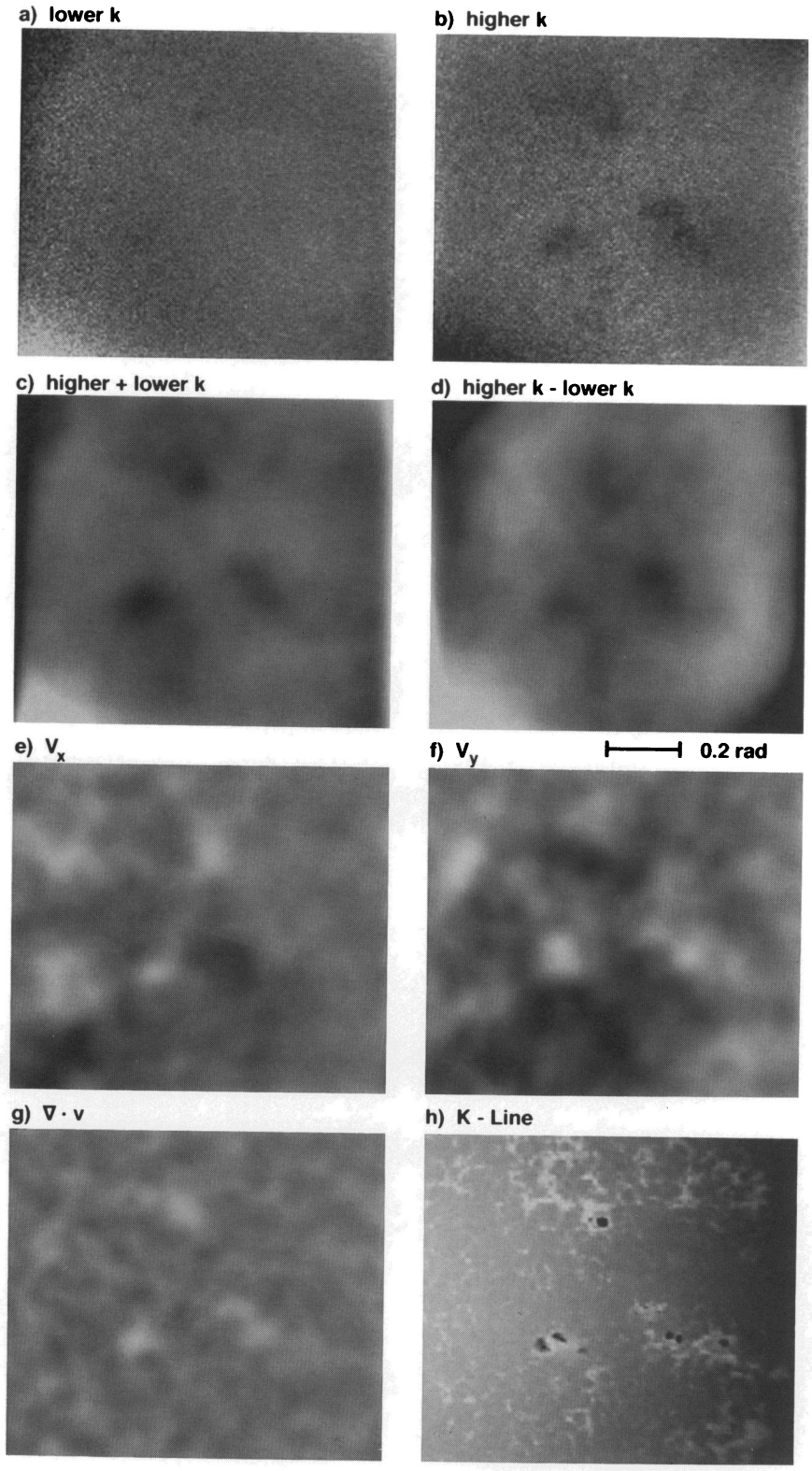

FIG. 3.—Acoustic power maps obtained by knife-edge spectral filtering. Frames (*a*) and (*b*) show acoustic power maps from power admitted by the mask in Fig. 2*b* (lower *k* domains) and its complement (higher *k*), respectively. Frames (*c*) and (*d*) show the sum ($b+a$) and difference ($b-a$), respectively, smoothed to a scale of 22,400 km. Frame (*d*) is normalized to register a difference of 0.1 times the total acoustic power (*c*) as white and -0.1 as black. Frames (*e*) and (*f*) show similarly smoothed Doppler maps for motion in the *x*- and *y*-directions, respectively. The gray scale in these frames is normalized to white for a flow of 250 m s^{-1} along the axis corresponding to the velocity component and to black for a flow of 250 m s^{-1} against. Frame (*g*) shows the divergence of the Doppler velocity. Frame (*h*) shows the K-line brightness averaged over the 50 hr period of the acoustic power maps.

© American Astronomical Society • Provided by the NASA Astrophysics Data System

1996ApJ...470..636L

Both the sum and difference images of the filtered data cubes (Figs. 2*c* and 2*d*) show strong signatures in regions of surface activity. Skipping to Figure 2*h*, we see the K-line image integrated over the entire 50 hr period of the acoustic power maps, showing the locations of three major active regions, AR 6431, AR 6432, and AR 6442, and a diminutive AR 6440 (see Solar Geophysical Data 1991). The locations of these regions are identified in Figure 1*d*. The local darkenings of the active regions in the total acoustic power (Fig. 3*c*) are due to superficial suppression of the chromospheric response to oscillations or from actual absorption of the oscillations, not phase perturbations due to refraction. However, the difference map (Fig. 3*d*) shows strong negative signatures (darkening) over the same regions. These difference signatures do indeed indicate phase perturbations, in this case a significant *downward shift* (decrease) in horizontal wavenumber, k, for the location of the activity. This would be the natural result of an increase in the sound speed or, alternatively, a Wilson depression, at the surface of the active region.

While surface magnetic structure generates a strong refractive signature, it presents serious practical difficulties from the perspective of depth discrimination. The phase contributions from various depths due to magnetic refraction are sharply weighted toward the extreme solar surface. Refractive perturbations expected from deep magnetic fields are simply undetectable. Shallower or stronger magnetic structure may induce a phase shift that is detectable in principle only to be swamped by weak plage at the surface. However, refraction is not the only contributor to the acoustic phase shift. Magnetic regions are generally seen to move with respect to their surroundings. This motion gives rise to Doppler effects, which manifest a phase shift far greater than that due to magnetic refraction at a great depth.

4. DOPPLER DIAGNOSTICS

Hill (1988) and Patron et al. (1995) have been using quasi-local Doppler analysis techniques effectively to determine horizontal velocity flows on a quasi-local scale, roughly 15° over the solar surface. They partitioned the solar surface into rectangular regions of this extent and obtained the Doppler velocity averaged over each region by the deviations of the centroids of its etalon rings from zero. This technique clearly shows signatures consistent with local flows on the scale of the 15° partition, a flow structure that varies sharply with depth.

Duvall et al. (1996) have recently created maps of both refractive and Doppler perturbations by active regions at the surface, using the techniques they have developed in time-distance helioseismology. They report wave travel time delays consistent with strong localized vertical flows, downdrafts, immediately below sunspots, of order 2 km s^{-1} in magnitude in the Bartol-NSO-NASA South Pole data. Kosovichev (1996a, 1996b) has applied tomographic inversion techniques to examine the depth dependence of the flows. D'Silva et al. (1996) present a formalism for modeling of the solar interior based on time-distance measurements.

It is important to realize that the knife-edge procedure we have described above is also sensitive to Doppler effects caused by local vertical flows to first order in the flow velocity. An understanding of the local quality of this signature is worth some effort, particularly in view of the apparent downflows found by Duvall et al. (1996). Vertical flows are somewhat orthogonal to the direction of this study, which is motivated by the particular advantages of horizontal Doppler diagnostics for the purpose of deep subsurface discrimination. We have therefore reserved an Appendix for a brief discussion of the local signature of vertical flows in Doppler knife-edge diagnostics. While we will continue to refer to the signature generated by the mask shown in Figure 2*b* as the "refractive" signature, one should keep in mind that it is indeed also quite responsive to local vertical flows. In fact, the refractive signature is also sensitive to horizontal flows, but only to second order.

5. PHASE CONTRIBUTION FUNCTIONS

We now propose to demonstrate a critical advantage that we think is offered by horizontal-flow diagnostics for the concern of depth discrimination. Our particular interest emanates from the fact that Doppler phase shifts contributed by deeper perturbations are comparable to those manifested by surface motions. This is mainly a result of Snell's law: While the vertical phase speed of the wave increases rapidly with depth, greatly reducing phase shifts from deep structure, the horizontal phase speed is constant. On the other hand, while phonons move much faster at the bottoms of their trajectories, their vertical group speeds go to zero as the trajectory becomes horizontal. Consequently, the time the phonon spends at the bottom of the trajectory is similar to that spent at the surface.

Our comparative discussion of refractive and Doppler diagnostics can be nicely quantified in the geometrical approximation by integrating the phase shift contributions from refractive and Doppler perturbations over the path, Γ, described by the phonons in the unperturbed medium. For a refractive perturbation, Δc, in sound speed, c, this path integral is

$$\Delta\phi = \int_\Gamma \Delta k\, ds = \int_\Gamma k \frac{\Delta c}{c}\, ds\,, \tag{1}$$

where $k = \omega/c$ is the magnitude of the wavevector, $\boldsymbol{k}$, in the unperturbed medium, and ds is the element of path length. For depth diagnostics, it is useful to express the path integral over depth, dz:

$$\Delta\phi \equiv \int_{z_s}^{z_t} P(z)dz\,, \tag{2}$$

where z_s and z_t are the depths of the endpoints of path Γ, and we will call P the phase contribution function. We let the vertical and horizontal components of the wavevector, $\boldsymbol{k}$, be k_z and k_h, respectively. Then,

$$\Delta\phi = \int_{z_s}^{z_t} k \frac{\Delta c}{c} \frac{k}{k_z}\, dz = \int_{z_s}^{z_t} k \frac{\Delta c}{c} \frac{1}{(1 - k_h^2/k^2)^{1/2}}\, dz\,. \tag{3}$$

The refractive perturbation, $\Delta c/c$, induced by a magnetic field, $\boldsymbol{B}$, is of order $\frac{1}{2}c_A^2/c^2 \sim B^2/8\pi\rho c^2$, where c_A is the Alfvén speed, and ρ is the density of the plasma, so the contribution function, P_B, for magnetic refraction is of order

$$P_B(z) = \frac{B^2}{8\pi\rho c^2} \frac{\omega}{c} \frac{1}{(1 - k_h^2 c^2/\omega^2)^{1/2}}\,. \tag{4}$$

The refractive phase contribution for a uniform magnetic field diminishes quickly with depth because of the sharp increase of both ρ and c. This is plotted in Figure 4*a* for 3 mHz waves with $l = 280$ ($n = 3$) for magnetic fields typical

© American Astronomical Society • Provided by the NASA Astrophysics Data System

1996ApJ...470..636L

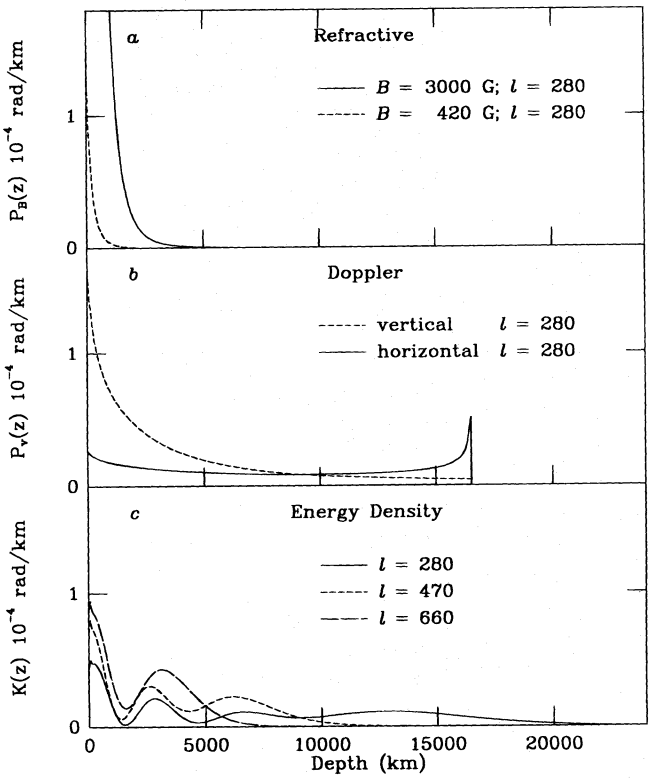

FIG. 4.—Phase contribution functions for (*a*) magnetic refraction and (*b*) vertical and horizontal Doppler motion in the limit of geometrical optics. Panel (*c*) shows the energy density of 3 mHz *p*-modes for wavenumbers, *l*, of 280, 470, and 660. These plots are normalized to give the same phase shifts, 0.19 radian, as the horizontal Doppler signature in (*b*), above.

of plage and sunspots at the solar surface. Prospects for refractive detection of deep subsurface fields are discouraging if not nil. A 3 kG flux tube 10,000 km in diameter submerged to a depth of 10,000 km induces a refractive phase shift of only $\sim 0^\circ.1$. This phase shift would be impractical to detect in the time interval we would expect such a configuration to last.

Because the sound speed increases roughly only as the square root of the depth in the convection zone, and the Doppler signature is of first order in velocity, Doppler phase shifts induced by flows, $\boldsymbol{v}$, offer far brighter prospects:

$$\Delta\phi = \int_\Gamma \frac{\boldsymbol{v}}{c} \cdot \boldsymbol{k}\, ds = \int_\Gamma k \frac{\boldsymbol{v}}{c} \cdot ds\,. \tag{5}$$

The phase contribution functions for vertical and horizontal flows are, respectively,

$$P_{v_z}(z) = \frac{v_z \omega}{c^2}\,, \tag{6}$$

and

$$P_{v_h}(z) = \frac{v_h}{c} \frac{k_h}{(1 - k_h^2 c^2/\omega^2)^{1/2}}\,. \tag{7}$$

$P_{v_z}(z)$ and $P_{v_h}(z)$ are plotted, respectively, as dashed and solid curves in Figure 4*b*, again for 3 mHz sound with $l = 280$ ($n = 3$), with v_z and v_h set uniformly to 500 m s^{-1}. The contribution function, P_{v_z}, for vertical flows remains strongly peaked toward the surface, although not nearly so much as for refractive perturbations. The contribution for horizontal flows, on the other hand, is considerably smaller at the surface but extends to the bottom of the phonon trajectory, a feature that has allowed us to explore the global rotational structure of the Sun deep into its interior over the last two decades. In this case, the phase shift integrated over the height spanned by P_{v_h} is $10^\circ.8$.

Where diffraction is important, the phase shift contributions for horizontal flows are better represented by eigenfunctions, in particular by their energy densities, which in the geometrical limit are inversely proportional to their vertical group velocities (see, e.g., Gough & Toomre 1983). Figure 4*c* shows these kernels, $K(z)$, for wavenumbers, *l*, of 280, 470, and 660. Their extents in depth are approximately proportional to $1/l^2$. The kernel for the smallest wavenumber ($l = 280$) extends downward to $\sim 16{,}000$ km. The largest ($l = 660$) extends only to ~ 4000 km.

Let us be clear that horizontal flow diagnostics are *not* generally more sensitive than vertical flow diagnostics. They are indeed *less* sensitive at all but the deepest levels. A major component of their strong practical advantage for subsurface diagnostics is in fact the *suppressed* surface sensitivity of the horizontal Doppler signature, which allows phase contributions from deeper perturbations to be significant.

6. THE HORIZONTAL DOPPLER SIGNATURE

A simple variation of the knife-edge mask shown in Figure 2*b* allows us to extract, statistically, just the horizontal Doppler profile along a specified direction. The Doppler masks utilize the principle that a horizontal flow, rather than contracting or expanding the etalon ring, to first order, simply moves the ring in *k*-space, a displacement

$$\Delta\boldsymbol{k} = \frac{k^2}{\omega}\boldsymbol{v} \tag{8}$$

for an extended flow, where $\boldsymbol{v}$ is the flow velocity. The spectral mask for motion in the positive *x*-direction (longitudinal motion), for example, is that shown in Figure 2*c*. Its analog for motion in the *y*-direction is shown in Figure 2*d*. The complements of these masks (not shown) are simple mirror reflections about the *y*-axis (Fig. 3*c*) and the *x*-axis (Fig. 3*d*), respectively. These masks accomplish for Doppler discrimination what the mask in Figure 3*b* does for refraction. They give us the optimum in local discrimination, at the expense of spectral discrimination.

The resulting signatures are shown in Figures 3*e* (*x*-velocity) and 3*f* (*y*-velocity), again smeared to the scale of 0.03 solar radii to eliminate high-frequency noise. These maps show a complex pattern of signatures, strongly associated with active regions visible at the surface. Other features are also seen that have no clear analog to surface activity. The signatures surrounding active regions are consistent with outflows. This is most easily recognized in the *y*-velocity signatures. A stronger signature in this direction may have something to do with the east-west elongation of the major active regions. The bright lobe above the center of AR 6442, for example, is the signature expected for a large region of northward-flowing gas. The relative darkening below is consistent with a southward flow. In either case, the proposed flow is away from the region. A calibration procedure, which we will describe in § 8, suggests that these flows are mostly submerged and have speeds of order 200 m s^{-1}.

© American Astronomical Society • Provided by the NASA Astrophysics Data System

1996ApJ...470..636L

While the procedure we are exercising is particularly designed to discriminate specifically horizontal flows, we have not by any means eliminated other physical or instrumental processes that could collaborate to give rise to such signatures without actual flows. It is important that these possibilities be explored more thoroughly than we have so far. Nevertheless, we will proceed from this point with the assumption that the horizontal Doppler signatures we have computed are indeed caused by horizontal flows. We will refer to the signatures themselves as flows. However, it is important keep in mind that we have not by any means exhausted mechanisms alternative to horizontal flows that could give rise to the signatures we have shown.

The considerations that determine the sensitivity of the horizontal Doppler signature to refractive perturbations or vertical motion are similar to those that determine the sensitivity of the refractive signature to horizontal motion (see Appendix). In fact, in an isotropic wave spectrum, the horizontal Doppler signature is totally insensitive to all orders to refractive perturbations or vertical flows that are horizontally uniform. This is a consequence of the antisymmetry of the Doppler masks, which generate a vector signature. Because horizontally uniform refractors or vertical flows have no preferred horizontal direction, their horizontal signatures must be null to all orders, for lack of a direction in which to point.

7. DOPPLER DIVERGENCE MAPPING

In principle (for quasi-static flows), a vertical velocity can be determined if the horizontal velocity field is discriminated with respect to depth. Since

$$\nabla \cdot \rho \boldsymbol{v} = 0 , \tag{9}$$

and we can determine the horizontal part, ∇_h, of the divergence from depth-resolved horizontal Doppler signatures, the upflow, v_z, can be derived from

$$\frac{\partial}{\partial z} \rho v_z = -\nabla_h \cdot \rho \boldsymbol{v}_h . \tag{10}$$

Since ρ is dependent almost entirely on depth alone, it can be taken outside of the horizontal divergence, ∇_h, on the right-hand side of equation (10). The left-hand side of equation (10) has two components:

$$\frac{\partial}{\partial z} \rho v_z = v_z \frac{\partial \rho}{\partial z} + \rho \frac{\partial v_z}{\partial z} . \tag{11}$$

We strongly suspect that the second can generally be neglected against the derivative of a density, ρ, that is strongly dependent on height, z. In that case,

$$v_z \frac{\partial \rho}{\partial z} = -\rho \nabla_h \cdot \boldsymbol{v}_h . \tag{12}$$

The upflow, then, approximates simply to

$$v_z = H \nabla_h \cdot \boldsymbol{v}_h , \tag{13}$$

where H is the e-folding height of the unperturbed solar medium at height z:

$$H = -1/(\partial \ln \rho / \partial z) . \tag{14}$$

Table 2 shows scale heights estimated at depths corresponding to the range of wavenumbers, l, whose kernels are plotted in Figure 4*c*. The equivalent vertical velocities, v_z, will generally be *considerably less* than the horizontal velocities we see, since H, even for the deepest layers that contribute to the Doppler signatures, is considerably less than the horizontal scale of the signatures we see. A map of the horizontal divergence, $\nabla_h \cdot \boldsymbol{v}_h$, from Figures 3*e* and 3*f*, is shown in Figure 3*g*, next to a K-line map of the same region, Figure 3*h*. This image shows clear positive (bright) signatures for all three of the major active regions covered by the acoustic power map. The horizontal divergence maps are considerably easier to compare with the K-line image for location of the equivalent flow with respect to the surface plage, and we will therefore examine them carefully. We will represent them in terms of their equivalent vertical velocity, as defined by equation (13). It is important to keep in mind that it is entirely the horizontal velocity diagnostic, not the vertical, that actually gives rise to this signature.

TABLE 2

CHARACTERISTIC DEPTHS

l Range	Representative l	Maximum Geometrical Depth (km)	H (km)
0–375	280	16,000	5500
375–565.....	470	8,000	2150
565–750.....	660	4,000	750

The horizontal outflows surrounding active regions suggested by the Doppler maps and their divergences appear geometrically somewhat contrary with the downflows that Duvall et al. (1996) report. Perhaps a greater difficulty than the conflict in direction is that the equivalent flows are so much smaller in magnitude. We will return to this point in § 7.

In Figure 5 (Plate 14), we compare refractive and Doppler maps and their respective divergences made before and after AR 6442 has erupted. The left and middle columns correspond to runs 1 and 2 in Table 1, respectively. The first interval ends 3.5 days before the eruption. The second ends 18 hr before the eruption, which begins on January 6 at 00:00 UT, the first sign of a sunspot appearing roughly 12 hr later. The posteruption interval is run 3 in Table 1. Figures 5*a*–5*c* (*top row*) show the K-line images integrated over the respective intervals in Table 1. Figures 5*d*–5*f* (*second row*) show the refractive signatures, Figure 6*f* identical to Figure 3*d*. Figures 5*g*–5*i* (*third row*) show the Doppler signatures for northward flow (northward, light; stationary, gray; southward, dark), Figure 5*i* identical to Figure 3*f*. Figures 5*j*–5*l* (*bottom row*) show the Doppler divergence signatures (outflow, light; stationary, gray; inflow, dark), Figure 5*i* identical to Figure 3*g*. The refractive signatures for runs 1 and 2 (Figs. 5*d* and 5*e*) are weak, perhaps because of insufficient statistics. The Doppler maps and their divergences, on the other hand, show significant signatures for active regions appearing at the surface in their respective epochs.

When we examine the Doppler maps and their divergences for a possible preemergence signature (Figs. 5*g*, 5*h*, 5*j*, and 5*k*) of AR 6442, we see the signature of a conspicuous southward flow just south of the emergence location in the flow map (Fig. 5*g*). While we do not doubt the statistical significance of this signature, the abundance of similar localized flow structures suggests that the coincidence of

© American Astronomical Society • Provided by the NASA Astrophysics Data System

1996ApJ...470..636L

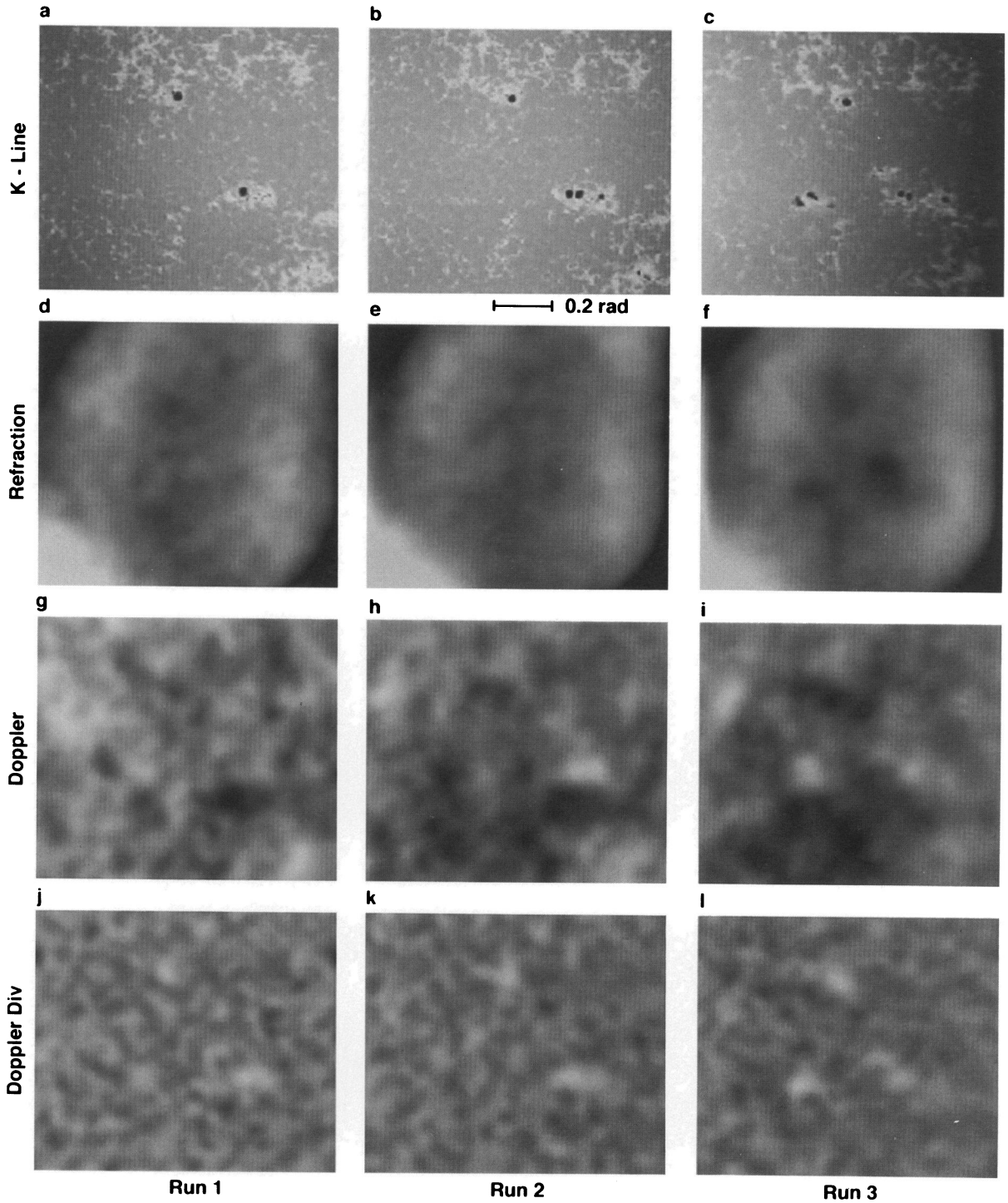

FIG. 5.—Acoustic signatures before and after emergence of AR 6442. Frames in cols. (1) and (2) apply to early and late preemergence. Frames in col. (3) (*far right*) apply to the postemergence. Frames (*a*)–(*c*) (row 1) show K-line images integrated over the periods corresponding to their respective columns (see Table 1). Frames (*d*)–(*f*) (row 2) show refractive signatures. Frames (*g*)–(*i*) (row 3) show the Doppler signatures for northward flow. Frames (*j*)–(*l*) (row 4) show the Doppler divergence signatures.

LINDSEY et al. (see 470, 640)

© American Astronomical Society • Provided by the NASA Astrophysics Data System

1996ApJ...470..636L

this flow with the location of AR 6442 could be an accident. Figure 5*j* suggests a weak positive divergence at the emergence site, i.e., an outflow. The equivalent vertical upflow is ~ 4.4 m s^{-1} (see Table 4). This signature is not apparent in Figure 5*k*, less than a day before AR 6442 appears at the surface.

8. DEPTH DISCRIMINATION

A simple partitioning of the acoustic power into three broad passbands in wavenumber separates the Doppler signatures into components whose respective wave modes probe to different depths. According to this interpretation, the horizontal Doppler signatures shown in Figure 5 emanate from a considerable range in depth. Figure 6 (Plate 15) shows the Doppler signatures for northward motion in three such passbands, chosen to be represented roughly by the wavenumbers appearing in the first column of Table 2: Figures 6*a*–6*c* show the K-line images integrated over the time intervals listed in the second and third columns of Table 1. Figures 6*d*–6*f* (second row, labeled Deep) show the Doppler divergence maps for low spatial wavenumbers, for l ranging from 0 to 375, again for runs 1 (*left column*), 2 (*middle column*), and 3 (*right column*). Figures 6*g*–6*i* (third row, labeled Intermed) show the signatures for l ranging from 375 to 565. Figures 6*j*–6*l* (bottom row, labeled Shallow) show the signatures for l ranging from 565 to 750, the effective seeing limit of the South Pole observations. The signal-to-noise ratio of these individual passbands is generally less than in the integrated acoustic power maps, because of the reduced statistics in the limited passbands. However, the images clearly show that the horizontal signatures that appear in Figures 3 and 5 are strongly dependent on l.

It should be clear from Figure 6 that for horizontal motion, the integrated Doppler signatures themselves are conspicuously strong functions of l. The outflows surrounding active regions appearing in Figures 3 and 5 are now seen to be predominantly a feature of the low wavenumbers (second row, labeled Deep), which explore down to 16,000 km or more. The result of this is a clear correlation between the deep-penetrating waves and surface activity. The Doppler maps at intermediate wavenumbers (third row, labeled Intermed) show substantially weakened outflow signatures, with the blatant exception of that surrounding newly emerged AR 6442 in Figure 6*i*.

While we do propose that the strong dependence of the Doppler signatures on wavenumber is the result of horizontal flows that increase rapidly with depth, we think it is, once again, wise to qualify this proposition, in that we have not nearly exhausted other possible superficial mechanisms that could give rise to such signatures. Nevertheless, we will proceed, for now, under the assumption that the signatures are simply the result of depth-dependent flows. It is important to keep in mind that under this interpretation, the horizontal Doppler signatures do *not* represent the flow simply at a single depth, or the deepest level, explored by the waves admitted by the spatial filter. They rather contain contributions integrated over the entire range of depths explored by the waves. We will make use of the approximation that the signatures shown in Figure 6 are simple vertical integrals of the velocity over depth, weighted by appropriate kernels with ranges approximately those shown in Figure 4*c*, as prescribed by Gough & Toomre (1983). We consider this approximation appropriate for flows whose horizontal extents are greater than the geometrical skip distance of the waves sampled.

One of the great assets of horizontal Doppler diagnostics is that it is straightforward to contrive a direct, realistic calibration of the signatures we obtain in terms of actual flow velocities. This is done simply by creating a modification of the data cube we have examined in which a selected region of the image, in this case a rectangular section, is artificially set into uniform motion with respect to the surrounding image. This procedure, applied to regions of different sizes perturbed with a variety speeds, allows us to calibrate the sensitivity of the Doppler knife-edge maps over all spatial scales. An example is shown in Figure 7 (Plate 16). We imposed a uniform northward motion of 500 m s^{-1} onto the region in the interior of the horizontal rectangle plotted in the K-line image shown in Figure 7*a*. The time series for this calibration is the 8 hr interval referred to as run 4 in Table 1. We note that the strong outflow northward from AR 6432 remains easily significant in this shortest of all time series for waves of low l. It is of order 200 m s^{-1}. Our calibrations show that the amplitude of the Doppler signature is nonlinear with the flow speed of the region, beginning to saturate for flows the width of that chosen in Figure 7 at speeds of roughly 500 m s^{-1}. Calibration computations made with rectangles of different widths show that a smaller feature of the same velocity as a larger one exhibits a signature that is smaller not only spatially but also in magnitude. The general outflow from AR 6431, visible in Figure 6*f*, culminates at a speed of 180 m s^{-1} at a distance of 0.05 radians (35,000 km) from the center of the active region (see Fig. 8). This is somewhat less than supergranular velocities observed at the solar surface.

In comparing the Doppler signatures of Figure 6 with those of Figure 7, the reader should notice that the gray scales for intermediate-l frames in Figure 6 are compressed to a narrower range than their low-l counterparts. The intermediate-l signatures are difficult to see when they are plotted on the same velocity scale as the low-l signatures. Table 3 lists calibrated maximum outflow velocities in the north-south direction from the active regions visible during run 3 (see Fig. 6). The calibrations assume that the flow velocity is uniform over the depth explored by the waves.

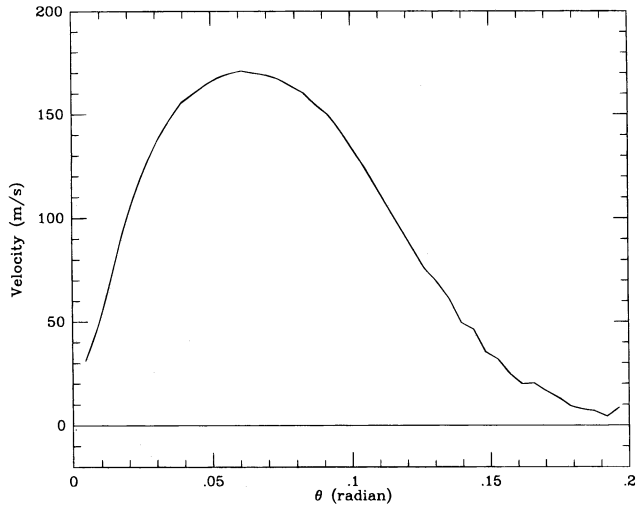

FIG. 8.—Profile of the radial flow rate of AR 6431 integrated along circles of constant radius, θ, from the center of the region.

© American Astronomical Society • Provided by the NASA Astrophysics Data System

1996ApJ...470..636L

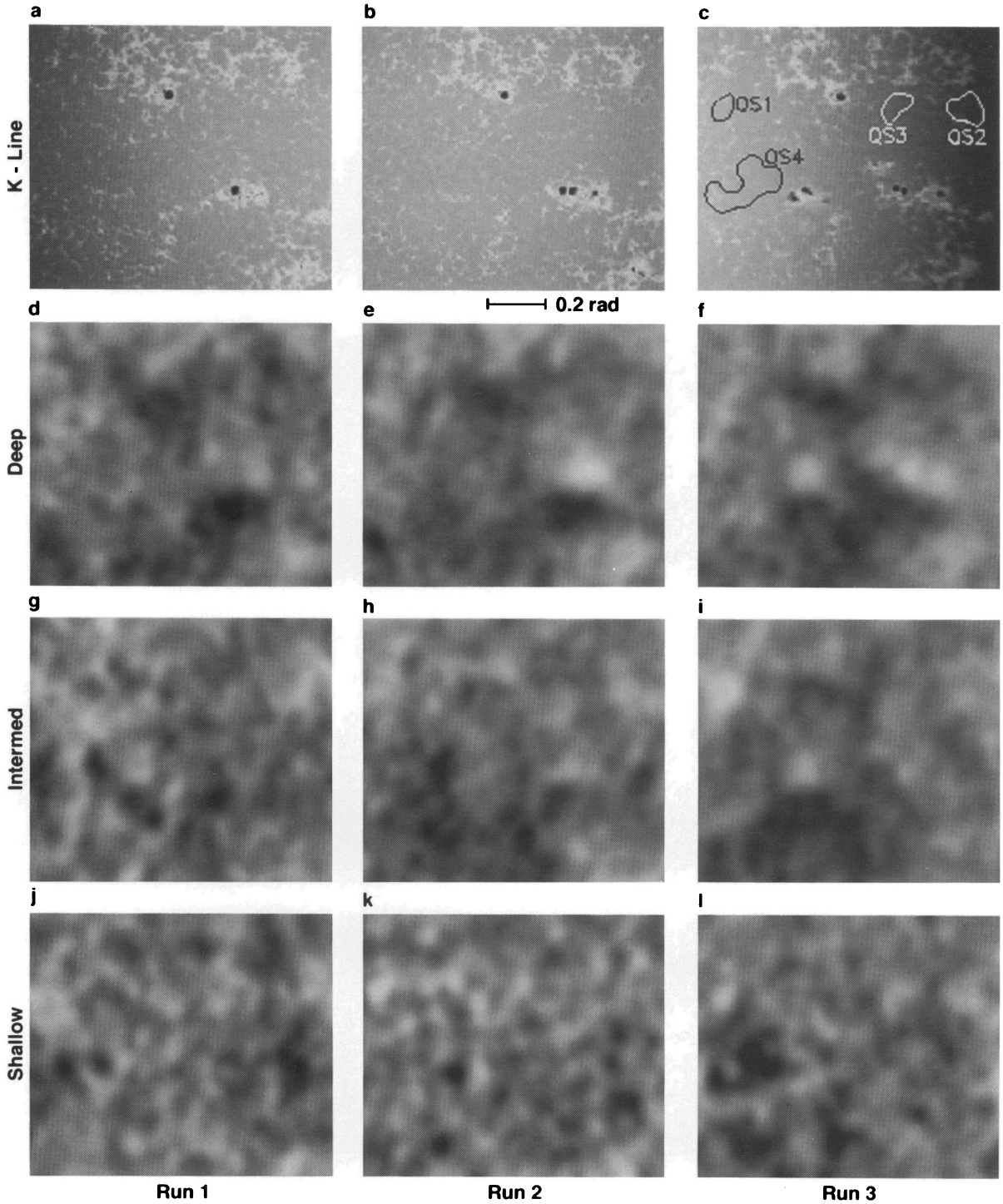

FIG. 6.—Maps of Doppler acoustic flow in the northward direction over a range of spatial wavenumbers. Frames in cols. (1) and (2) apply to early and late preemergence. Frames in col. (3) apply to postemergence. Frames (*a*)–(*c*) (row 1) show K-line brightness integrated over the respective intervals. Frames (*d*)–(*f*) (row 2) map the Doppler divergence for l in the range 0–375. For frames (*g*)–(*i*) (row 3) l lies in the range 375–565. For frames (*j*)–(*l*) (row 4) l lies in the range 565–750. The approximate depths explored by waves in these ranges are listed in Table 2.

© American Astronomical Society • Provided by the NASA Astrophysics Data System

1996ApJ...470..636L

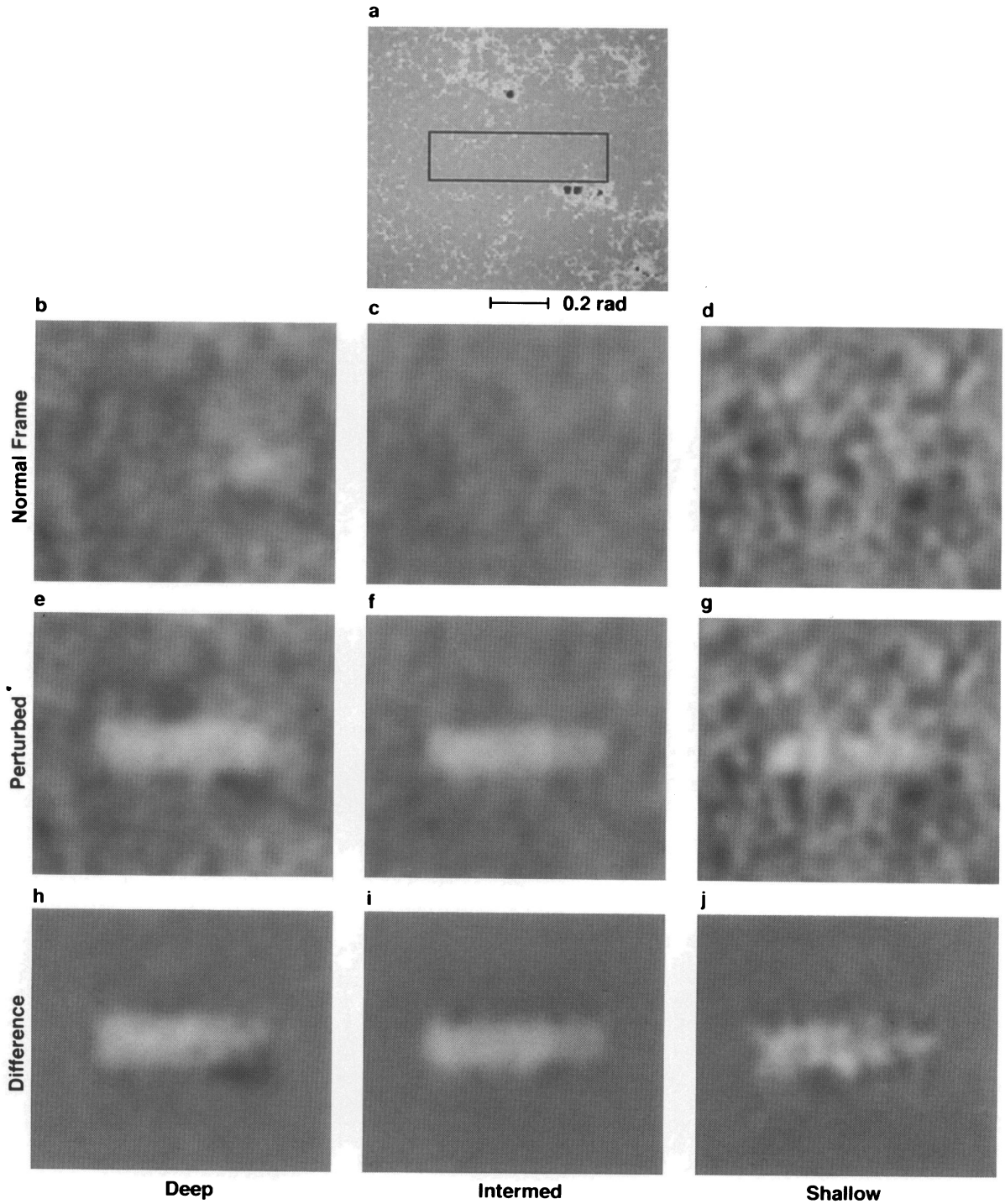

FIG. 7.—Calibration of the northward component of the flow velocity is illustrated for low-l (*left column*), intermediate-l (*middle column*), and high-l (*right column*). An 8 hr data cube (run 3 in Table 1) was altered by artificially drifting the region in the interior of the rectangle plotted in frame (*a*) northward throughout the time series. The second row of the figure (labeled Normal) shows Doppler signatures for y-velocity without the perturbation. The third row (labeled Perturbed) shows the Doppler signatures with a drift velocity of 500 m s^{-1} imposed in the rectangle interior. The bottom row (labeled Difference) is the difference of the Perturbed Signature minus the Normal.

LINDSEY et al. (see 470, 641)

© American Astronomical Society • Provided by the NASA Astrophysics Data System

1996ApJ...470..636L

TABLE 3

MAXIMUM OUTFLOW VELOCITIES

Region (NOAA)	l Range	Velocity (m s^{-1})
AR 6442	0–375	227 ± 19
	375–560	133 ± 18
	560–750	89 ± 14
AR 6440	0–375	184 ± 19
	375–560	78 ± 18
	560–750	87 ± 16
AR 6432a	0–375	234 ± 20
	375–560	83 ± 18
	560–750	17 ± 18
AR 6432b	0–375	165 ± 20
	375–560	24 ± 19
	560–750	36 ± 25
AR 6431	0–375	227 ± 19
	375–560	111 ± 18
	560–750	19 ± 18
QS 1	560–750	164 ± 24
QS 2	560–750	185 ± 45
QS 3	560–750	153 ± 40
QS 4	560–750	251 ± 24

The "errors" listed in the third column are rms variations in the background in selected quiet regions containing no indication of structure. (These rms deviations are *not* the standard deviations generally used to establish confidence.)

When we examine the Doppler signatures of the most superficial waves, the high-l range, the outflows surrounding active regions essentially disappear, and we encounter other features having no clear counterpart in surface activity. The calibration (Fig. 7), integrated over only an 8 hr period, shows a strong stochastic pattern with flow speeds of order ± 300 m s^{-1} on a horizontal scale not much greater than the supergranulation (Figs. 7*d* and 7*g*). As we will explain in the next section, this pattern appears to be the result of noise.

Returning to Figure 6, which is integrated over a 49 hr period, roughly the lifetime of the supergranulation, the stochastic pattern subsides somewhat, to show some larger scale, if somewhat slower, flows (bottom row, labeled Shallow). A close examination of the Shallow and Intermediate rows strongly suggests that some of these features are persistent. A compact northward flow (bright feature), identified as QS 1 in Figure 6*c*, appears in Figure 6*l*. It has clear counterparts in Figure 6*h*, 6*j*, and 6*k* and somewhat diffuse counterparts in Figures 6*g* and 6*j*. This flow seems to develop and persist in the quiet Sun over the several day interval of runs 1–3. Figure 6*l* also shows two other north-flowing regions, identified in Figure 6*c* as QS 2 and QS 3. The rightmost of these, QS 2, has significant analogs in Figures 6*g*, 6*h*, and 6*j*. The other, QS 3, has an approximate analog in Figure 6*j*, and possibly a weak one in Figure 6*h*. Regions QS 1–3 appear to be part of a general band of northward flows apparent in Figures 6*j*–6*l* that lie in the quiet Sun just south of the southern border of the northern activity band, particularly where this band is populated only by diffuse plage. On the other hand, an extended

TABLE 4

DOPPLER DIVERGENCE SIGNATURES

Region (NOAA) (1)	l Range (2)	Run (3)	Area (mSun[a]) (4)	Equivalent Vertical Flow (m s^{-1}) (5)	Flux (6)
AR 6431	0–375	1	0.712	49.43 ± 14.76	0.0352 ± 0.0088
	0–375	2	1.406	39.92 ± 11.45	0.0561 ± 0.0096
	0–375	3	0.792	55.55 ± 11.78	0.0440 ± 0.0074
	375–560	1	0.758	4.18 ± 1.83	0.0032 ± 0.0011
	375–560	2	0.831	6.60 ± 2.40	0.0055 ± 0.0015
	375–560	3	0.820	4.93 ± 1.70	0.0040 ± 0.0011
	0–750	1	0.509	8.96 ± 3.05	0.0046 ± 0.0015
	0–750	2	0.886	9.39 ± 2.81	0.0083 ± 0.0019
	0–750	3	0.780	10.32 ± 2.32	0.0081 ± 0.0014
AR 6432a	0–375	1	0.733	60.69 ± 14.76	0.0445 ± 0.0089
AR 6432	0–375	2	1.607	49.99 ± 11.45	0.0803 ± 0.0103
AR 6432a	0–375	3	0.817	40.92 ± 11.78	0.0334 ± 0.0075
AR 6432b	0–375	3	0.806	34.43 ± 11.78	0.0277 ± 0.0075
AR 6432	375–560	1	1.240	2.87 ± 1.83	0.0036 ± 0.0014
AR 6432a	375–560	2	0.810	6.90 ± 2.40	0.0056 ± 0.0015
AR 6432a	375–560	3	0.759	4.43 ± 1.70	0.0034 ± 0.0010
AR 6432b	375–560	3	1.193	1.73 ± 1.70	0.0021 ± 0.0013
AR 6432a	0–750	1	1.043	8.35 ± 3.05	0.0087 ± 0.0022
AR 6432	0–750	2	1.375	9.63 ± 2.81	0.0132 ± 0.0023
AR 6432a	0–750	3	0.789	7.27 ± 2.32	0.0057 ± 0.0015
AR 6432b	0–750	3	1.754	3.23 ± 2.32	0.0057 ± 0.0022
AR 6442	0–375	3	0.476	59.61 ± 11.78	0.0284 ± 0.0057
	375–560	1	1.105	4.59 ± 1.83	0.0051 ± 0.0014
	375–560	2	1.015	0.73 ± 2.40	0.0007 ± 0.0017
	375–560	3	0.936	7.57 ± 1.70	0.0071 ± 0.0012
	0–750	1	0.903	4.37 ± 3.05	0.0039 ± 0.0020
	0–750	2	0.928	1.70 ± 2.81	0.0016 ± 0.0019
	0–750	3	0.835	10.69 ± 2.32	0.0089 ± 0.0015
AR 6440	375–560	3	0.563	4.49 ± 1.70	0.0025 ± 0.0009
	0–750	3	0.570	7.12 ± 2.32	0.0041 ± 0.0012

NOTES.—6432a: left lobe; 6432b: right lobe. Run 1: Early preemergence of AR 6442; Run 2: Late preemergence of AR 6442; Run 3: Postemergence of AR 6442.

[a] One-thousandth of the total solar surface area.

© American Astronomical Society • Provided by the NASA Astrophysics Data System

1996ApJ...470..636L

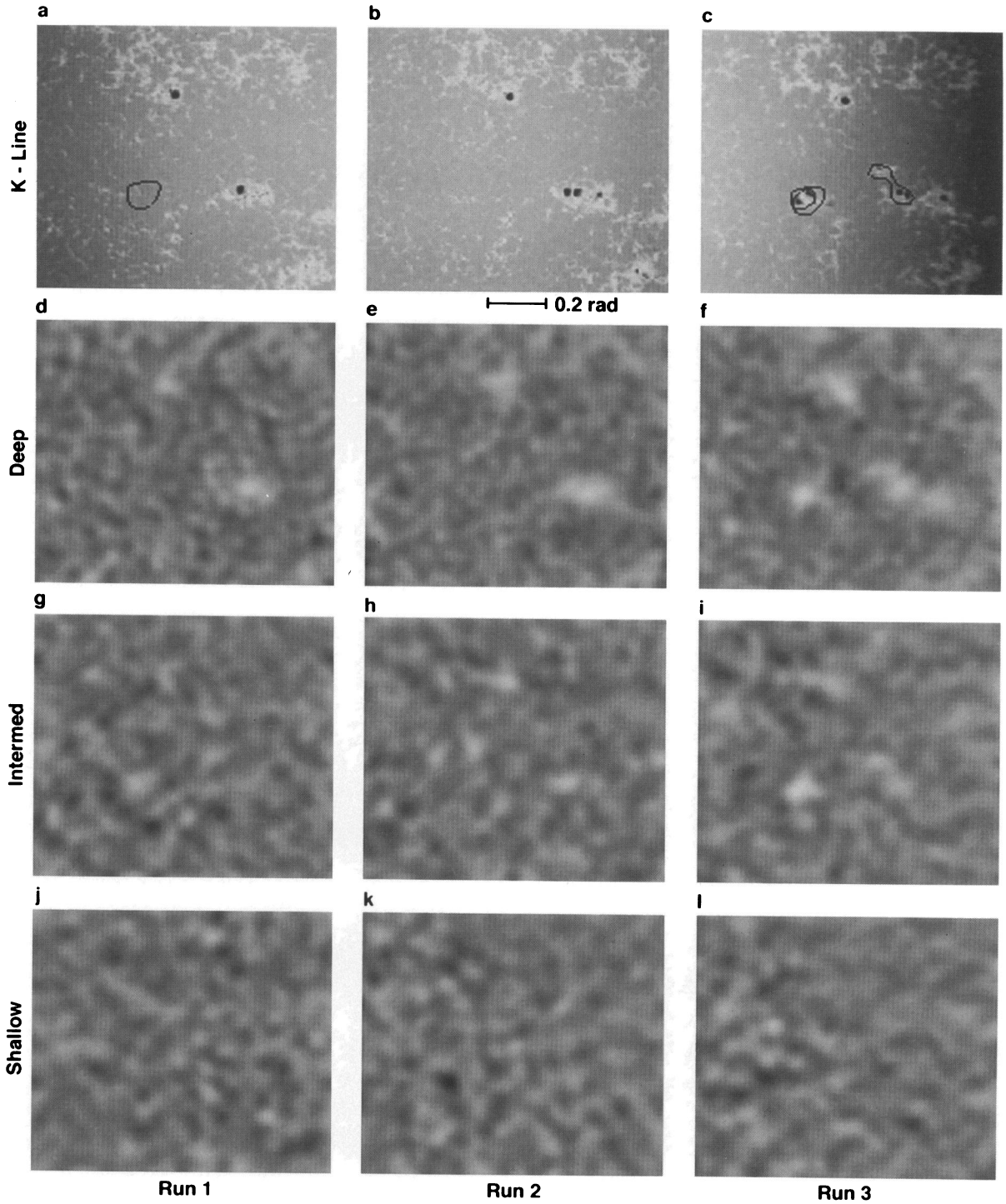

FIG. 9.—Doppler acoustic divergence maps over a range of spatial wavenumbers. As in Fig. 6, frames in cols. (1) and (2) apply to early and late preemergence. Frames in col. (3) apply to postemergence. Frames (*a*)–(*c*) (row 1) show K-line brightness integrated over the respective intervals. Frames (*d*)–(*f*) (row 2) map the Doppler divergence for l in the range 0–375. For frames (*g*)–(*i*) (row 3) l lies in the range 375–565. For frames (*j*)–(*l*) (row 4) l lies in the range 565–750.

© American Astronomical Society • Provided by the NASA Astrophysics Data System

1996ApJ...470..636L

southward flow indicated by a dark signature in Figure 6*l* is identified in Figure 6*c* as QS 4. Compact vestiges of this flow appear in Figures 6*j* and 6*h*. This southward flow lies just north of the northern border of the southern activity band, which in that neighborhood is populated by plage that is somewhat more diffuse and intermittent than its counterparts lying north of QS 1–3. These superficial flows in the quiet Sun into the active region bands are similar in speed (but, of course, not in mass flux) to the deep outflows surrounding large active regions. Their maximum speeds are listed at the bottom of Table 3.

A dark feature with an adjoining bright feature on its right appears in Figure 6*k* in the location of AR 6442, soon to emerge. It is possible that this flow is associated with QS 4, as it is not far to the right (west) of the right extreme of that flow.

Figure 9 (Plate 17) shows the Doppler divergence signatures of the same regions in the same time intervals whose northward flows were shown in Figure 6. These images make it apparent that only relatively deep outflows from active regions have conspicuous divergences, which require supporting upflows. The flow signatures of the shallowest waves are apparently significant but do not manifest large divergences. The strong dependence of the active region flows on wavenumber is unmistakable in the divergence maps. The active region signatures we see here continue to increase sharply with the depth explored by the waves sampled. Moreover, this strong dependence itself varies from one region to another. The mature active regions (AR 6431 and AR 6432) have a strong signature only for the lowest *l*s (second row, labeled Deep). They seem to be characterized by relatively deep flows. The newly emerging active region, AR 6442, on the other hand, has a particularly strong signature at intermediate *l* (third row, Fig. 9*i*), suggesting a shallower outflow. While AR 6442 gives us the most spectacular example, it is not the only case. A careful examination of AR 6440 (also Fig. 9*i*), a small region that erupts on the periphery of AR 6432, shows a signature that matches that of the much larger, but older, region in the intermediate range of *l*. This pattern is very striking and strongly suggests rapid evolution in deep interior flow structure.

The possible preemergence signature of AR 6442 appears to reside entirely in wavenumbers in the intermediate range of *l*, 375 to 565 (Fig. 9*g*: third row, labeled Intermed), if anywhere. Curiously, few if any of the shallow flows visible in Figure 6 (bottom row, labeled Shallow) appear to have a significant divergence signature (same row, Fig. 9). Outflows and inflows, which would require supporting up- or downflows, appear to avoid depths less than 4000 km below the solar surface.

Table 4 shows calibrated integrations of the Doppler divergence features visible in Figure 9. The features selected were averaged over areas listed in column (4) and their average equivalent vertical flow rates over those areas listed in column (5). The "errors" listed in column (5) are, as in Table 3, not standard deviations but rather rms variations in the background in selected quiet regions containing no indication of structure. The product of columns (4) and (5), an equivalent flux, is listed in column (6). Here we have assumed, given a point surrounded by a region of 0.5 mSun in area, that points lying outside of that region are statistically independent of the center point. Here, the unit "mSun" denotes 1/1000 of the total surface area of the Sun (see Table 4). We have used this to assign standard deviations to the flux measurements, which are listed as the errors in column (6). It is these errors that should be used to judge the statistical significance of the measured flow.

9. DISCUSSION

The horizontal Doppler signatures we have examined have shown us some very striking, unexpected features:

1. Evidence for outflows surrounding active regions with moderate speeds, up to several hundred meters per second.
2. Evidence for a rapid evolution of these proposed outflows, particularly the submergence of the flow to great depths as the region matures.
3. Evidence of extended superficial flows in the quiet Sun between the active region bands, generally pouring into the active region bands.
4. Some suggestion of a preemergence signature of AR 6442, which would be roughly confined to depths in the range 4000–8000 km.

We have not thoroughly explored other mechanisms that may give rise to the signatures we have presented. However, our calibrations clearly indicate that, whatever other effects may give rise to these signatures, the diagnostics we have contrived are indeed sensitive to horizontal flows at the level of a few tens of meters per second. The flows that we propose to surround active regions appear to extend to great depths. The profiles we have obtained here open a broad range of topics and questions concerning the subsurface structure and hydrodynamics of solar activity.

The indication of outflows from active regions by itself is not particularly surprising. Mature active regions are known to develop outflowing "moats" (Meyer et al. 1974) at their surfaces. Mass flux conservation suggests that the moat flow must continue outside the outer radius of the moat in some fashion, and we do indeed see extended outflows. However, the apparent tendency for this extended flow to submerge as the active region matures is most puzzling. The hydrodynamics of active region formation and evolution are complex. The Doppler signatures strongly suggest that the moat is the single superficial manifestation of an outflow that is otherwise farther submerged than when the region is forming and no moat is visible (see Fig. 10).

Some thought needs to be expended on the compatibility between the outflows implied by the knife-edge diagnostics and the strong downflows suggested by the correlation time delays reported by Duvall et al. (1996). A large horizontal *inflow* is needed to feed a downflow such as that inferred by Duvall et al. (1996). Consider a downflow, v_z, of 2 km s^{-1} whose horizontal extent is defined roughly by a radius, R, of 10,000 km, for example (see Kosovichev 1996b). If we suppose that the divergence of the horizontal inflow, $\nabla_h \boldsymbol{v}_h$, that feeds the downflow is distributed roughly over this radial extent, then it should be of order v_h/R. In that case, equation (13) imposes the need for a horizontal flow speed of

$$v_h = \frac{R}{H} v_z \,. \tag{15}$$

For an inflow localized in the upper 4000 km of subphotosphere, the photospheric scale height, H, is roughly 750 km (see Table 2). This requires a horizontal inflow rate,

© American Astronomical Society • Provided by the NASA Astrophysics Data System

1996ApJ...470..636L

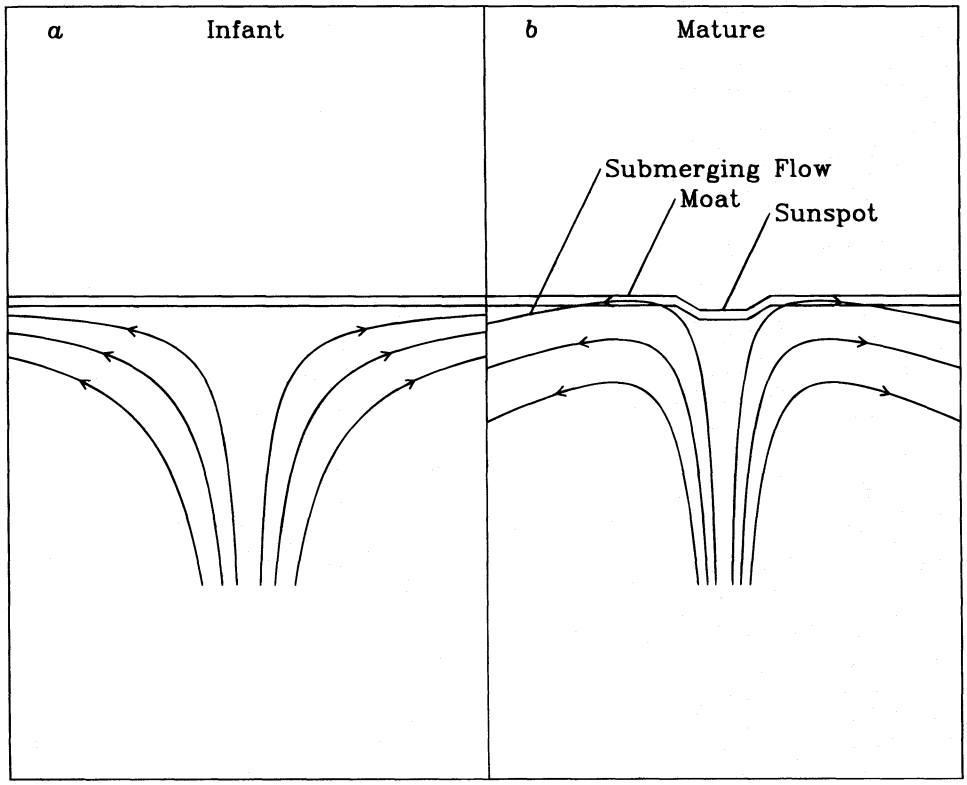

FIG. 10.—Schematic diagram of (*a*) superficial preemergence outflow and (*b*) extended submerging outflow outside of the surface moat surrounding a mature active region.

v_h, of about 25 km s^{-1} to supply the mass to replace the down-flowing material. This is only one of a large number of possible flow geometries. However, this pessimistic example illustrates the difficulty in contriving a flow configuration that would accommodate rapid downflows without imposing relatively shallow horizontal flows near the sunspot of at least several kilometers per second. While it is possible that the horizontal Doppler diagnostic is sensitive to other processes besides horizontal flows and these could invalidate our interpretation in terms of submerged outflows, it is difficult to propose how such a process would work so that inflows 1–2 orders of magnitude greater than those of the calibration configurations we have examined would be hidden or supplanted by signatures consistent simply with comparatively modest outflows. In summary, a strong downflow, an extended outflow, and an outflowing moat appear to require at least a flow configuration that is quite complex if not a little bit diabolical. We have made no attempt to include a down-flowing region in Figure 10. However, the large time delays seen by Duvall et al. (1996) are very interesting, and flow geometries that could explain both the Doppler knife-edge signatures and the time-distance time delays need to be considered more carefully than we have here.

Is it possible that the Doppler effects Duvall et al. (1996) are seeing are in fact due to the same horizontal flows that we see? These, at least, would produce time delays of the same sense as downflows. In the polytropic approximation, for a constant outflow of velocity v, the time delay, τ, for an annulus of radius ρ satisfies the relation

$$\rho = \frac{\gamma - 1}{4\pi} g\tau^2 \pm v\tau \,, \tag{16}$$

where addition applies to outgoing waves and subtraction to ingoing. The first term on the right is 48 minutes if ρ spans a 10° annulus surrounding the active region. To first order in v, the travel time difference between outgoing and ingoing is simply

$$\Delta\tau = \frac{4\pi}{\gamma - 1}\frac{v}{g} \,. \tag{17}$$

If we take v to be 90 m s^{-1}, the horizontal flow rate the knife-edge signatures indicate if averaged over a 10° (0.17 radian) annulus (see Fig. 8), then equation (16) gives a time travel difference, $\Delta\tau$, of 6 s, much too small to account for the $\sim$1 minute measured by Duvall et al. (1996).

If either the horizontal Doppler signatures or the large time delays seen by Duvall et al. (1996) are to be explained by means other than flows, it is important to consider processes that are preferential as to the direction of time, e.g., processes that are statistically irreversible. Is it possible, for example, that the correlation time delays reported by Duvall et al. (1996), rather than being the result of actual travel time differences, are instead due to thermal relaxation in the local K-line chromosphere? Such an effect would, perhaps, delay only the response of the chromosphere in K-line brightness to the wave, imposing no significant effect on the actual wave hydrodynamics in the solar interior. The relaxation time needed to cause the correlation time lags seen by Duvall et al. (1996) would be of order 30 s, phase-shifting a 5 minute oscillation by 36°. Lites, Chipman, & White (1982) measure phase shifts between brightness variations and velocity for Mg I λ8542, and the calcium infrared triplet lines, Ca II λ8542 and Ca II λ8498, in the quiet Sun, which form low in the chromosphere roughly where the wings of the K-line form. They find phase departures (from

© American Astronomical Society • Provided by the NASA Astrophysics Data System

1996ApJ...470..636L

the $-90°$ for evanescent adiabatic oscillations) ranging from $-25°$ for Mg I λ8542 and $-16°$ for Ca II λ8542, to $+14°$ for Ca II λ8498. Lites (1986) measures a phase departure of $-45°$ for the Ca II H line in sunspot umbrae. While phase shifts spanning this range need to be carefully studied, it is important to understand that they can explain the time delays seen by Duvall et al. (1996) without strong downflows only if they are different, by something like 36° *between the active region chromosphere and the quiet Sun.*

Similarly, a gradient in the relaxation time as one progresses from the quiet Sun into an active region would result in an acoustic signature indistinguishable, as far as we can see, from that of a horizontal flow, and the equivalent velocity of such a flow would tend to increase with depth (roughly in proportion to the speed of sound). The role of chromospheric relaxation should be relatively easy to check using Doppler data, such as from the Global Oscillations Network Group (GONG) or the *Solar Heliospheric Observatory* (*SOHO*).

Another irreversible process to consider is the mechanism whereby sunspots absorb a large fraction of the acoustic waves that encounter them. M. F. Woodard (1996, private communication) suggested the possibility that this may introduce time delay asymmetries that imitate vertical flows. He is investigating this prospect from a range of different perspectives.

Braun et al. (1996) anticipate that absorption of acoustic waves should give rise to a spurious inflow signature of up to 30 m s^{-1} near the sunspot because of the increase of the sunspot's absorption coefficient with wavenumber for l up to about 350. This is about an order of magnitude less than the outflow velocities equivalent to the signatures we are seeing and opposite in direction.

The Doppler maps we have presented have difficulty resolving flows on the scale of the supergranulation. Figures 7*d* and 7*g* show a stochastic pattern for shallow waves equivalent to rapid superficial flows over an 8 hr time interval that have a horizontal scale not much greater than that of the supergranulation. The stochastic flows in Figure 7*d* span a range of approximately ± 300 m s^{-1}. Figures 7*c* and 7*f* show a much weaker stochastic background with a range of approximately ± 100 m s^{-1}. However, we do not see a significant correlation between the high-l stochastic pattern and the low-l. Moreover, when we examine high-l Doppler maps made from consecutive 8 hr time series, we see no significant cross-correlation for features on the scale of the stochastic pattern. Because of this, we now think that the stochastic patterns that appear in the high-l Doppler maps of Figure 7 are largely if not entirely the result of noise. This also suggests that the rapid flows that do characterize the supergranular convection at the solar surface do not extend very deep. The relatively limited Doppler signatures on this scale suggest that the flow velocities are high only perhaps in the upper 1000–2000 km of the solar subsurface. One should be careful not to venture the same proposition for mass flux, which could be large and quite deep without giving rise to a significant Doppler acoustic signature. This null result should not be regarded as a particular disappointment. It appears that higher l waves are needed to study the supergranulation, and high-quality observations of these are already being given to us by *SOHO*.

Is the preemergence signature of AR 6442 real? We do not know. If it is, then its appearance in the intermediate range of l is consistent with the relatively superficial signature of the early postemergence signature. However, it is puzzling that such a signature should appear days in advance of the eruption and become substantially invisible the day before. We need to examine more emerging regions to engage the prospect of preemergence diagnostics seriously.

Is there an analogy in time-distance helioseismology to the horizontal Doppler signature? The correlation time lags measured by Duvall et al. (1996), between a reference point and a surrounding concentric annulus, do not particularly discriminate between horizontal and vertical flows, and, we think, are relatively insensitive to the average horizontal flow over the annulus. D'Silva (1996) describes other techniques based on two-point correlations. However, the annular configuration has an enormous statistical advantage over the two-point correlation, particularly for large separations (Duvall et al. 1993). We think that a straightforward extension of the annular correlation would secure the horizontal Doppler signature in particular, with no loss in statistical advantage: It is important to reflect that the annulus need not be concentric with the reference point. Where local horizontal flows are important, the correlation can be determined as a function of the *offset* between the point of reference and the center of the annulus. If both the offset and the time delay are then chosen to optimize the correlation, then the offset will substantially contain the horizontal Doppler information, we propose. T. L. Duvall (1996, private communication) has recently obtained horizontal Doppler signatures by a simpler method that divides a concentric annulus into four quadrants and compares time delays for travel to and from the reference point in the appropriate quadrants. He finds outflows from active regions that tentatively appear similar to those presented here.

We think that local helioseismology has a great deal to contribute to our understanding of solar interior MHD and fluid motion. In the short term, we need more statistics on active region evolution, something that the GONG and *SOHO* projects are about to make available. We need to follow the Doppler signatures of active regions not only from before their births but until some time after they die—if that is actually what they do when they disappear from the surface. We need to examine the outflow profiles at greater and shallower depths, and we need cleaner observations. The high-quality and extensive temporal coverage the GONG and *SOHO* projects are now giving us may make possible the holographic and modeling techniques proposed by Lindsey & Braun (1990), Braun et al. (1992), Brown (1991), and D'Silva et al. (1996). However, it is also important that we carefully examine processes other than subsurface flows that could give rise to the signatures we are seeing. It is quite possible, as far as we can judge, that we will be able to examine magnetic structure at great depths and see the solar dynamo at work. To be realistic, we think that literally only the extreme surface of this new possibility has been explored so far.

We thank Karen and Jack Harvey for their sponsorship and management of our research program in Local Helioseismology at the Solar Physics Research Corporation. We thank Jacques Beckers for accommodating the special needs of our program at the National Solar Observatory. We thank Jack Harvey (again), Tom Duvall, and Martin Pomerantz for making this possible with their high-quality

© American Astronomical Society • Provided by the NASA Astrophysics Data System

1996ApJ...470..636L

South Pole observations. We thank Tom Duvall (again) for comments on the manuscript, suggestions and scientific insight. C. Lindsey, D. Braun, S. Jefferies, and M. Woodard enjoy visiting appointments at the National Solar Observatory, supported by the National Science Foundation (NSF). This research was supported by NSF grants ATM 92-14714, AST 94-96171, OPP-9219515, DPP-8917626, ONR grant N00014-91-J-1040, and NASA grant NAGW-4143.

APPENDIX A

THE VERTICAL FLOW SIGNATURE OF REFRACTIVE DIAGNOSTICS

At first glance it would appear that the knife-edge diagnostic described in § 2 would be relatively insensitive to vertical flows. This is indeed true if the flow is horizontally extended. In that case, the phase shift introduced by Doppler effects to a phonon propagating one way, say upward, through an upward-moving layer, are canceled, to first order, by the same phonon having been forced to travel downward through a region of similar upflow nearby. The refractive signature can respond to first order only to a horizontally confined upflow. More explicitly, if $\boldsymbol{v}$ is vertical, equation (5) becomes

$$\Delta\phi = \int_\Gamma k \frac{v_z}{c}\, dz\,, \tag{18}$$

and if v_z depends only on z, then the path integral along the down-going section of Γ ($dz < 0$) cancels that along the up-going ($dz > 0$). For $\Delta\phi$ to be significant, the upflow needs to have substantial structure on a horizontal scale less than the "skip distance," the horizontal span of the geometrical optical path, Γ, between surface encounters. In the convection zone, these paths are approximately simple cycloids, and the distance between reflections is approximately π times the depth explored by the waves. For upflows whose horizontal scale is similar to their vertical scales, for example, there must exist paths, Γ, satisfying the foregoing condition.

Given that a vertical flow manifests a refractive signature, it is useful to consider the spatial quality of such a signature. In particular, we expect a positive phase shift, $\Delta\phi$, for a phonon propagating upward through a local upflow, having traveled downward through stationary gas some distance away. On the other hand, one should notice that waves traveling the opposite direction will accumulate the opposite, a negative phase shift, and this opposite phase perturbation will be manifested at the surface roughly a skip distance away from the local upflow. What this means is that the positive signature for the region above the local upflow is surrounded, roughly a skip distance away, by a halo of opposite signature such that the total signature integrated over a locality securely encompassing the skip radius around the upflow is null, just as it is uniformly for a uniform upflow (to first order in flow velocity). This is an important difference between the "refractive" signature of a local upflow and that of a truly refractive perturbation, whose halo a skip distance from its center reenforces the signature directly above the perturbation.

The sensitivity of refractive knife-edge diagnostics to local vertical flows is apparently comparable to that of the time-distance helioseismic techniques of Duvall et al. (1996). However, the knife-edge signatures cannot distinguish between Doppler and refractive phase shifts as the time-distance measurements of Duvall et al. (1996) do. We reiterate that the term refractive signature is a misnomer that we put up with for convenience. The refractive signature can be indicative of vertical flows. Indeed, if the signature manifests a significant dependence on horizontal wavelength, then we think that this is probably the case.

REFERENCES

Bogdan, T. J., & Braun, D. C. 1995, in Helioseismology: Proc. Fourth *SOHO* Workshop, ed. J. T. Hoeksema, V. Domingo, B. Fleck, & B. Battrick (Noordwijk: ESA), 31
Bogdan, T. J., Brown, T. M., Lites, B. W., & Thomas, J. H. 1993, ApJ, 406, 723
Born, M., & Wolf, E. 1975, Principles of Optics (Oxford: Pergamon Press)
Braun, D. C. 1995, ApJ, 451, 859
Braun, D. C., Duvall, T., & LaBonte, B. J. 1988, ApJ, 335, 1015
Braun, D. C., Fan, Y., Lindsey, C., & Jefferies, S. J. 1996, in preparation
Braun, D. C., Lindsey, C., Fan, Y., & Jefferies, S. M. 1992, ApJ, 392, 739
Brown, T. M. 1991, Sol. Phys., 128, 133
Calley, P. S., & Bogdan, T. J. 1993, ApJ, 402, 721
D'Silva, S. 1996, ApJ, in press
D'Silva, S., Duvall, T. L., Jefferies, S. M., & Harvey, J. W. 1996, ApJ, in press
Duvall, T. L., D'Silva, S., Jefferies, S. M., Harvey, J. W., & Schou, J. 1996, Nature, in press
Duvall, T. L., Jefferies, S. M., Harvey, J. W., & Pomerantz, M. A. 1993, Nature, 362, 430
Gough, D. O., & Toomre, J. 1983, Sol. Phys., 82, 401
Hill, F. 1988, ApJ, 333, 996
Hollweg, J. V. 1988, ApJ, 335, 1005
Keppens, R., Bogdan, T. J., & Goossens, M. 1994, ApJ, 436, 372
Kosovichev, A. G. 1996a, Bull. Astron. Soc. India, in press
———. 1996b, ApJ, 461, L55
Lindsey, C., & Braun, D. 1990, Sol. Phys., 126, 101
Lindsey, C., Braun, D., & Jefferies, S. J. 1996, in preparation
Lites, B. W. 1986, ApJ, 301, 992
Lites, B. W., Chipman, E. G., & White, O. R. 1982, ApJ, 253, 367
Lou, Y.-Q. 1990, ApJ, 350, 452
Meyer, F., Schmidt, H. U., Weiss, N. O., & Wilson, P. R. 1974, MNRAS, 169, 35
Patron, J., Hill, F., Rhodes, E. J., Korzennik, S. G., & Cacciani, A. 1995, ApJ, 455, 746
Sakurai, T., Goossens, M., & Hollweg, J. V. 1991, Sol. Phys., 133, 247
Spruit, H. C., & Bogdan, T. J. 1992, ApJ, 391, L109
Toner, C. G., & LaBonte, B. J. 1993, ApJ, 415, 847
Zernike, F. 1935, Z. Tech. Phys., 16, 454

© American Astronomical Society • Provided by the NASA Astrophysics Data System